Electron Dynamics in the High-Density Laser-Wakefield Acceleration Regime

B.S. Nicks,[1] S. Hakimi,[1] E. Barraza-Valdez,[1] K.D. Chesnut,[1] G.H. DeGrandchamp,[1] K.R. Gage,[1] D. B. Housley,[2] G. Huxtable,[1] G. Lawler,[3] D.J. Lin,[1] P. Manwani,[3] E.C. Nelson,[1] G.M. Player,[1] M.W.L. Seggebruch,[1] J. Sweeney,[1] J.E. Tanner,[1] K. A. Thompson,[2] and T. Tajima[1]

[1)] *University of California, Irvine*

[2)] *University of California, San Diego*

[3)] *University of California, Los Angeles*

(Dated: 11 August 2020)

The electron dynamics of laser wakefield acceleration is examined in the high-density regime, including the dependence on the plasma density and the amplitude and pulse length of the laser. In the very high (near-critical) density regime, electrons are accelerated by the ponderomotive force followed by the electron sheath formation, resulting in a flow of bulk electrons. This regime exhibits qualitatively distinct features from the low-density LWFA case, and an index for differentiating these regimes is proposed. Applications of these properties to medical conditions are considered.

I. INTRODUCTION

Laser Wakefield Acceleration (LWFA)[1] is a compact method to accelerate charged particles to high energies that was first purposed by Tajima and Dawson[2] in 1979. While the accelerating electric field in a conventional linear accelerator is limited by the breakdown threshold of the device walls, plasma-based accelerators can access far higher electric fields, owing to the inherently broken-down nature of plasma. Consequently, plasma-based accelerators can access far higher accelerating gradients than those available to conventional accelerators, reaching potentially GeV per cm or higher. The original proposal for LWFA called for a laser intensity of 10^{18} W/cm^2, but this regime of intensity only became accessible after the invention of Chirped Pulse Amplification (CPA)[3], and LWFA was experimentally verified shortly thereafter[4,5]. Since then, many more experiments demonstrated this technique in different regimes, and the field has grown steadily.

Accelerators have many applications in our current society, one of the most important being their use in radiation therapy. Particle beams in the form of X-rays, electrons, and protons can be used to treat cancer. These energetic beams can ionize molecules which in turn damage cellular DNA. Cells with damaged DNA can not reproduce and are eliminated through natural processes in the body. The type of beam used depends highly on the size and location of cancer being treated. For example, while X-rays and electrons deposit most of their energy in the surface layers, protons can be controlled to deposit their energy at a specific depth due to Bragg peak phenomena[6,7], dramatically reducing damage to healthy cells. Proton therapy contends with other limitations, however[8].

Current accelerators used for radiation therapy use traditional linear accelerator technology. To produce an electron or X-ray beam, electrons from an electron gun are accelerated and guided through waveguides using electric fields and magnets. These electrons can eventually hit a target and produce X-rays. However, the material breakdown limits of linear accelerators tend to require that these machines be large and costly. The typical electron energy needed for radiation therapy is between 5-20 MeV. LWFA techniques can accelerate electrons to these energies in micron to millimeter scale lengths. Such a high acceleration gradient reduces the size and cost of these machines, consequently increasing their availability.

Research in the use of LWFA to generate electron beams for medical applications has proceeded for more than two decades now. Initially, these efforts focused on the generation of high-quality electron beams with energies roughly in the range 6-25 MeV, as would be applicable for conventional, external sources of radiation for cancer therapy[9–15]. Recent innovations in the field of fiber lasers has offered a new leap forward in this effort: the Coherent Amplification Network (CAN)[16], in which many individual micron-scale fiber lasers are coherently combined and amplified to provide both high-rep rate and high power. In such a scheme, laser accelerators could possibly be further compactified as to be viable even for endoscopic applications. If electrons can be generated inside of a patient's body (or in an intraoperative[12,13] fashion), the desired energy of these accelerated electrons (and X-rays converted from them) is much lower than those of typical, high-energy LWFA (MeV and above), as they need not traverse healthy tissues before reaching the tissues to be treated. Consequently, we wish to study LWFA in the high-density, low-intensity regime. In contrast to high-energy LWFA regimes, the low-energy LWFA regime is less explored in detail. Subsequently we focus on this regime with intended applicability to fiber lasers, emphasizing the fundamental physics and taking only the beginning steps towards medical applications.

In LWFA a clear path to MeV-range electrons exists through increasing the plasma density. Electron energy gain is given by $\Delta\mathcal{E} = 2g(a_0)m_ec^2(n_c/n_e)$, where $a_0 = eE_0/m_e\omega_l c$ is the normalized vector potential of the laser pulse with E_0 and ω_l representing the electric field and frequency of the laser. Here e, m_e, and c are electron charge, electron mass, and speed of light respectively.

If the function $g(a_0)$ takes the form of the ponderomotive potential, then $g(a_0) = \sqrt{1+a_0^2} - 1$[17], but generally here $g(a_0)$ is taken to be unity at $a_0 = 1$. The electron energy gain is proportional to the ratio of n_c, the critical plasma density defined by the laser frequency, to n_e, the plasma or electron density. If the value of this ratio is near 1, the electron energy gain is on the order of MeV or lower. (The critical density for the commonly used 800 nm Ti:Sapphire laser is $1.73 \times 10^{21}\text{cm}^{-3}$.) In the following, we study the scaling laws of electron energy gain $\Delta\mathcal{E}$ over the parameters of plasma density, intensity a_0, and laser pulse duration, as well as investigate the mechanics of electron acceleration in the high-density regime.

II. ACCELERATION IN THE HIGH-DENSITY REGIME

If the plasma density is near the laser critical density, the typical physics of LWFA transitions into a qualitatively distinct regime where analytic extensions of conventional wakefield physics[18] may become insufficient. In particular, the laser group velocity $v_g = c\sqrt{1-n_e/n_c}$, which is approximately equal to the wake phase velocity, approaches zero, and the pump depletion and dephasing lengths, which are on the order of $L_d \sim L_p \sim \lambda_p a_0^2 (n_c/n_e)$, become shorter than the plasma wavelength $\lambda_p = 2\pi c/\omega_p$ for $a_0 = 1$. The length scale of laser interaction with the plasma becomes better described by the plasma skin depth, given by c/ω_p. Consequently the laser-plasma interaction primarily occurs within one λ_p, and the laser couples significantly to the bulk motion of the plasma, which is characterized by the plasma thermal velocity $v_T = \sqrt{T/m}$, where T and m here are most relevantly those of the electrons but can in general correspond to ions or electrons. This situation contrasts starkly with that of low-density wakefield physics, in which the laser (having $v_g \approx c$) penetrates deeply into the plasma without coupling to the bulk motion. In this case the phase velocity of the wakefield becomes $v_{ph} = v_g \approx c$, allowing the laser to build a long wake train ($L_d \sim L_p \gg \lambda_p$) robustly and stably. When electron injection occurs, the wakefield can then skim a small population of electrons from the bulk and accelerate them to high energies. This sharp divide in fundamental physics requires examination of the high-density regime on its own terms and a qualitative understanding apart from that of conventional wakefield acceleration.

The differences between the qualitative physics of the high- and low-density cases, which respectively represent waves of low and high phase velocity relative to the plasma thermal velocity, extends to many general features of plasma physics. For waves with $v_{ph} \sim v_T$, the wave couples to the bulk thermal motion of the plasma, typically producing macro-instabilities and turbulence. Plasma structures are thus fragile to such waves, and may disintegrate from wave-induced transport. In contrast, waves with $v_{ph} \gg v_T$ do not couple to the bulk thermal motion of the plasma, and the plasma and wave are insulated from each other. With regard to the wave fields, the wave can then reach a robust saturation amplitude before particle trapping begins to occur. In this limit, the wave trapping velocity[19] becomes approximately equal to the wave phase velocity, leading to the characteristic Tajima-Dawson saturation amplitude $E_{TD} = m\omega v_{ph}/q$, where ω is the wave frequency and m and q are respectively the mass and charge of the relevant species. At this saturation amplitude, wave-particle interaction manifests as the acceleration of a tail of extremely fast particles, and the thermal distribution remains intact. The free energy of such a wave can even build plasma structures, in contrast to the case of low phase velocity. The plasma is durable against the wave, rather than fragile. Because the original LWFA concept was built on this high phase-velocity paradigm and departs from the sheath-forming, high-density regime[20], most or all works on LWFA have to date avoided the high-density (low phase-velocity) regime. Thus it is the purpose of the present work to first qualitatively distinguish these two regimes and then quantitatively characterize the differences in their most important dynamics. To do so, we isolate the longitudinal spatial dynamics and show their overwhelming influence on the departure of the physical characteristics of the above two regimes.

Returning to LWFA, the interaction of the laser with the plasma in these two contrasting regimes of high and low density has a convenient analogy in tsunami waves in a certain property of the wave dynamics. In the open ocean, where the water depth is great, tsunami waves propagate with a fast phase velocity and thus do not couple to stationary objects. Boats in the ocean, for instance, may move slightly in the transverse direction (vertically), but are not otherwise affected. The ocean water thus remains serene and "blue". Let us call this the "blue" regime of a tsunami. Near the shore, however, the increasingly shallow water causes the phase velocity of the wave to slow down (the shallow-water dispersion is given by its phase velocity $v_{ph} = \sqrt{gh}$, where g is the gravitational acceleration and h is the water depth, while in deep water the wave has $v_{ph} = \sqrt{g/k}$ with wavenumber k[21]), which leads to amplification and steepening of the wave until breaking occurs. The slow velocity of the wave near the shore then causes catastrophic trapping of stationary objects. Additionally the slow wave velocity couples with turbulence created by wave breaking to create transport on the sediment bed. Significant amounts of sediment quickly pass into the wave, creating visibly "black" water from the clean, "blue", offshore starting wave. Let us call this transformed wave a "black" tsunami. As a further consequence of turbulence, an effective viscosity causes momentum transport of the sediment. In the case of a more typical wakefield with $n_c \gg n_e$, somewhat analogous to the above described tsunami transformation with respect to the phase velocity, the bulk plasma remains almost entirely unaffected, leaving the wave "blue". In the high-density case, however, the wave phase velocity becomes sufficiently low

to begin scraping particles from the bulk distribution, resulting in "black" waves. In the analysis below, we casually apply these labels of "black" and "blue" for the high- and low-density wakefield regimes, respectively, as well as "grey" for the transitional regime.

To study the distinct physics of the high-density regime and its transition from the low-density regime, we employ the particle-in-cell (PIC) code EPOCH. Establishing a firm conceptual foundation in this physics first requires understanding of the case where one spatial dimension (and three velocity dimensions) are employed. This work is also primarily interested in the phase-space structure of accelerated electrons, rather than the real-space evolution of the laser pulse and wakefield. Thus, 2D phenomena such as strong self-focusing[22] and hole-boring of ions[17] are not examined. Such 2D effects beget other effects, such as collapse of the laser pulse[23], which can lead to an expanding cloud of electrons. These effects and others, such as magnetic vortex physics[24] and prominent ion motion, are also more typical of the regime of ultra-intense pulses, which is not an emphasis of this work. Peak ion energy achieved in this study is typically 0.1 MeV. Comparisons to ion-acceleration schemes, such as TNSA and RPA[25,26] are not addressed here.

For this simulation setup, the laser is injected from vacuum through an impedance-matching boundary into a uniform plasma of electrons and protons with temperature $T = 100$ eV. Such a configuration represents a simple and idealized case that can be analyzed easily, yet contains the crucial physics. This scheme contrasts with some past efforts in which the laser was injected into a density ramp that peaked near the critical density[23]. In this case, the laser pulse collapsed before reaching the region of critical density owing to important 2D effects. Here a uniform density is used to examine the physics of laser-plasma interaction at the full critical density. Additionally, as opposed to initializing the laser inside the plasma, the vacuum injection scheme may better reflect the experimental reality for the high-density case near the critical density if we take as a target a porous nanomaterial[27–29], for which the injected laser has $v_g \sim 0$. Care is taken that the essential laser-plasma physics is unchanged between the cases of vacuum injection and laser initialization inside the plasma. The laser is taken to have a vacuum wavelength of one micron and a resonant pulse length with functional dependence $E_y = E_0 \sin(kx - \omega t - \phi)h(x,t)$, where $h(x,t)$ is a resonant flat-top profile, and ϕ is an optional phase. By default ϕ is set to zero. (The oscillatory component of E_y thus grows from zero as the laser enters the simulation domain.) A resonant pulse is half the length of the plasma wavelength λ_p. The remaining laser and plasma quantities are then controlled through two parameters: the laser intensity a_0 and the critical density ratio n_c/n_e. Position in the simulation domain is indicated by the value x. The laser is injected at $x = 0$, and "forward" and "backward" correspond to the directions $+\hat{x}$ and $-\hat{x}$, respectively.

A resonant laser pulse in a plasma near the critical density ($n_c/n_e \leq 2$) must necessarily be sub-cycle, or at most single cycle. While sub-cycle lasers have been demonstrated experimentally[30,31], such a setup would be generally difficult to implement, particularly in a fiber laser[16]. Instead, a long, self-modulating pulse would be much more amenable to a fiber laser application, as is discussed in section IV. For simplicity and consistency with the low-density regime, however, here a resonant pulse is used. It will be shown that with a longer pulse the essential physics remains unchanged. Another concern arising from a sub-cycle laser pulse is the influence of the initial laser phase ϕ. Care has been taken to ensure that choice of ϕ does not affect the essential physics, even for $n_c/n_e = 1$. One can show analytically that the initial ponderomotive kick felt by the electrons lies in the same direction as the laser Poynting vector, creating a tendency toward uniformity across various values of ϕ.

With the simulation scheme established, the first step in examining the high-density regime is then to approach it from the better-understood low-density limit. Such an approach is done by scanning over the density values $n_c/n_e \in [1, 10]$, taking an intensity of $a_0 = 1$. The maximum energy gain $\Delta\mathcal{E}$ for electrons in LWFA, where 1D theory applies, is given by $\Delta\mathcal{E}/m_e c^2 \approx 2(n_c/n_e)$ for $a_0 = 1$. The maximum acceleration found over the scan of density values, shown in Fig. 1, agrees well with this proportionality. For at least the highest-energy electrons this scaling is evidently obeyed up to the critical density. However, a crucial assumption of this expression for $\Delta\mathcal{E}$ is that the wakefield amplitude remains constant in time. For low densities ($n_c/n_e \gtrsim 10$), this assumption begins to break down significantly, resulting in longer distance required for acceleration and somewhat lower final electron energy than that given by $\Delta\mathcal{E}$ above.

We may now take a closer look at each regime. For the "blue" wave case of $n_c/n_e = 10$, Fig. 2 shows a snapshot of the electron phase space overlaid with the longitudinal and laser electric fields. The train of accelerated electrons is clearly visible, and the highest-energy electrons reach the theoretically expected momentum of $p_x^{max} \approx m_e c\sqrt{(2g(a_0)n_c/n_e)^2 - 1}$[2]. The coherent wake structure is also seen, with saturation in the longitudinal field reaching the expected value[32] of $E_{max}/E_{TD} \approx 0.4$. The wake is gradually diminished as it imparts energy to the electrons, but recovers after the dephasing length $L_p \approx 8\lambda_p$.

In contrast, the "black" wave case of $n_e = n_c$, shown in an initial stage in Fig. 3a and final stage in Fig. 3b, exhibits quite different behavior. Here, $v_g = 0$, and $L_{p,d} \lesssim \lambda_p$, restricting the laser-plasma interaction to within one plasma wavelength. The long train of trapped electrons becomes replaced by streams of low-energy ($\Delta\mathcal{E} \sim 100$ keV) electrons ejected from the site of oscillation roughly every plasma period. The generation of a net bulk momentum indicates the presence of an effective viscosity. The mechanics of acceleration in the case of $n_c/n_e \approx 1$ represent a distinct qualitative regime than that of the typical wakefield case of $n_c/n_e \gg 1$.

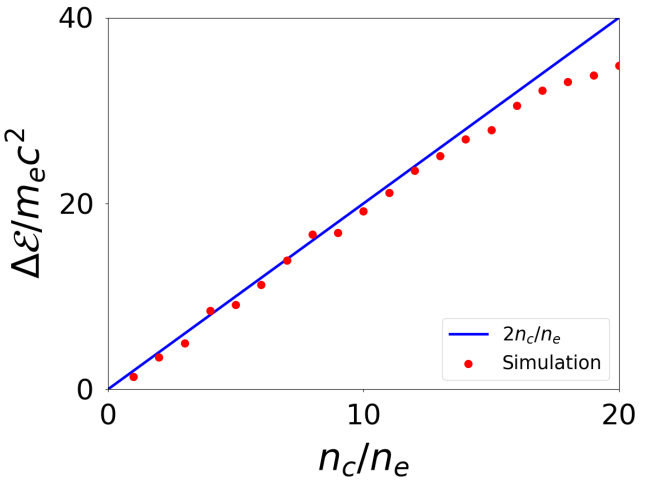

FIG. 1: Scaling of the normalized maximum electron energy with density n_c/n_e for the laser intensity $a_0 = 1$, compared with the theoretical expression for the energy gain of electrons $\Delta\mathcal{E}$ in LWFA.

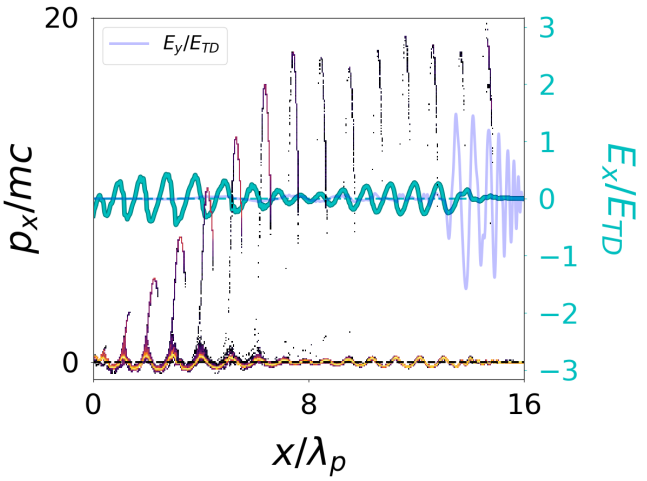

FIG. 2: A snapshot of the electron phase space p_x vs. x (heat-map, with warmer colors representing higher density) and longitudinal E_x (green) and laser E_y (translucent blue) fields for the somewhat typical wakefield case of $n_c/n_e = 10$ ("blue") and $a_0 = 1$ after the electron acceleration has saturated. The plasma wavelength is given by $\lambda_p = 2\pi c/\omega_p$. The forward edge of the laser pulse is at $x/\lambda_p = 16$.

Having $v_g \ll c$, the laser couples strongly to the bulk motion of the electrons upon entering the plasma, pushing out a much larger spike in electron density ($\delta n_e/n_e \approx 3.5$) than in the low-density case while the ions are not substantially affected. This density spike creates a longitudinal electric field of approximately twice the strength as in the low-density case and causes the reflection of a substantial portion of the laser. This powerful initial kick to the plasma establishes a strong longitudinal oscillation of electrons in the range $0 \le x \le \lambda_p$.

The strong restoring electric field then causes this density spike to rebound, and simultaneously those electrons having $v_x \ll c$ are accelerated to near the expected energy $\Delta\mathcal{E}$ from 1D wakefield theory. The restoring motion of the initial electron density spike expels many electrons through the left edge of the domain, establishing a sheath[20] at the boundary of strength comparable to the initial laser amplitude. This sheath, representing the remnants of the original electron density spike, subsequently oscillates longitudinally. Because the sheath oscillation has phase velocity $v_{ph} = 0$, owing to $n_c/n_e = 1$, these oscillations couple strongly to the bulk motion of the electrons. Every period, the sheath dredges electrons from the bulk distribution and accelerates them to a range of low energies (< 100 keV). This acceleration launches the electrons in the forward direction, forming streams in phase space. The presence of the sheath insures that these electron streams travel nearly exclusively in the forward direction. (If the sheath is not present, a significant number travel backwards.) Figure 3a, a snapshot of the electron phase space and fields zoomed to the range $0 \le x \le \lambda_p$, shows the beginning of this process, where the first streams of accelerated electrons, as well as secondary, fin-like streams, are visible. As the oscillation continues, more streams accumulate, building up the phase-space distribution in Fig. 3b, which shows the full simulation domain. In the later stages, the electron acceleration becomes increasingly turbulent until the oscillation is finally exhausted after about 30 plasma periods. The full evolution of the sheath and electron density is shown in Fig. 4. While the individual energy of the accelerated electrons is low compared to that of the low-density case, the total energy imparted to the accelerated electrons can potentially be higher. This total imparted energy represents about 12% of the total injected laser energy, though it should be kept in mind that such efficiency values are inherently rough estimates in a 1D simulation. This understanding of the electron dynamics associated with sheath formation should also be useful for the understanding of related ion acceleration dynamics[1,6]. The sheath acceleration mechanism observed here is also reminiscent of that in cases examined previously[17].

The transition to sheath acceleration from typical wakefield acceleration represents a sharp division of qualitative regimes of wakefield physics. Pursuing this point further, we can attempt to find a quantitative means of discriminating these regimes. Visually comparing figures 3 and 2 suggests a quantitative index related to the entropy of the phase-space structure; the electron phase space in the low-density case is highly ordered compared with that of the high-density case. In general however, comparing the entropy of two distributions also requires an accounting for the mean kinetic energy of the distributions. Thus, as an index for discriminating the "blue" and "black" regimes, we propose

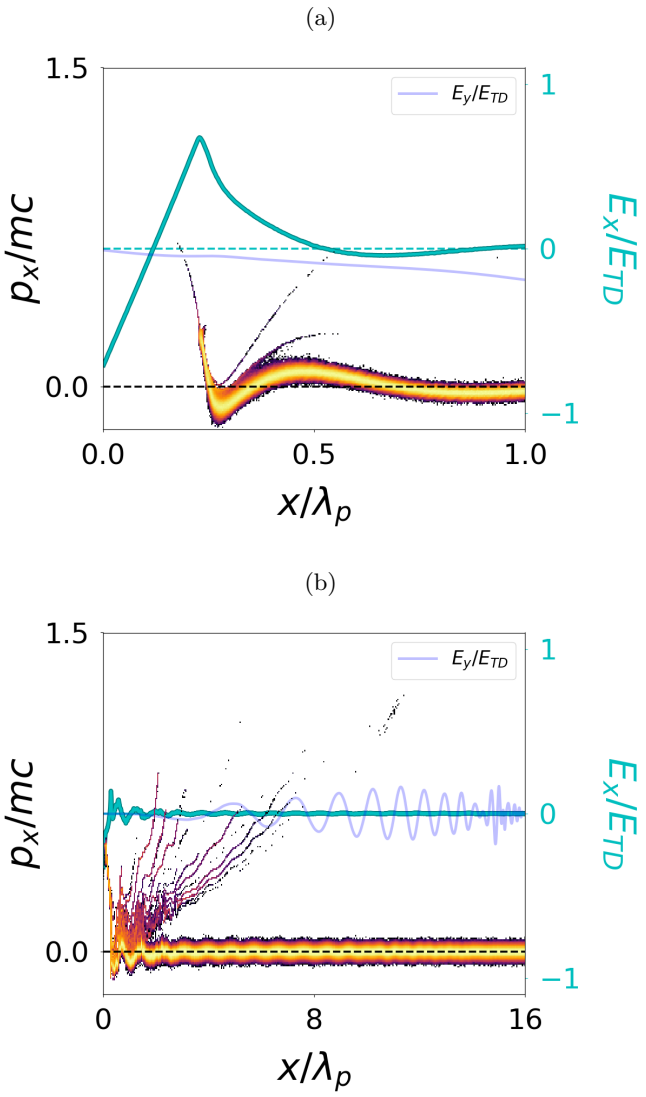

FIG. 3: Electron phase space and field structure of the high-density ("black") case $n_c/n_e = 1$ with laser intensity $a_0 = 1$ at early (3a) and later (3b) stages. The development of the electron streams is observed. Figure 3a is zoomed to $0 \leq x \leq \lambda_p$ from (3b).

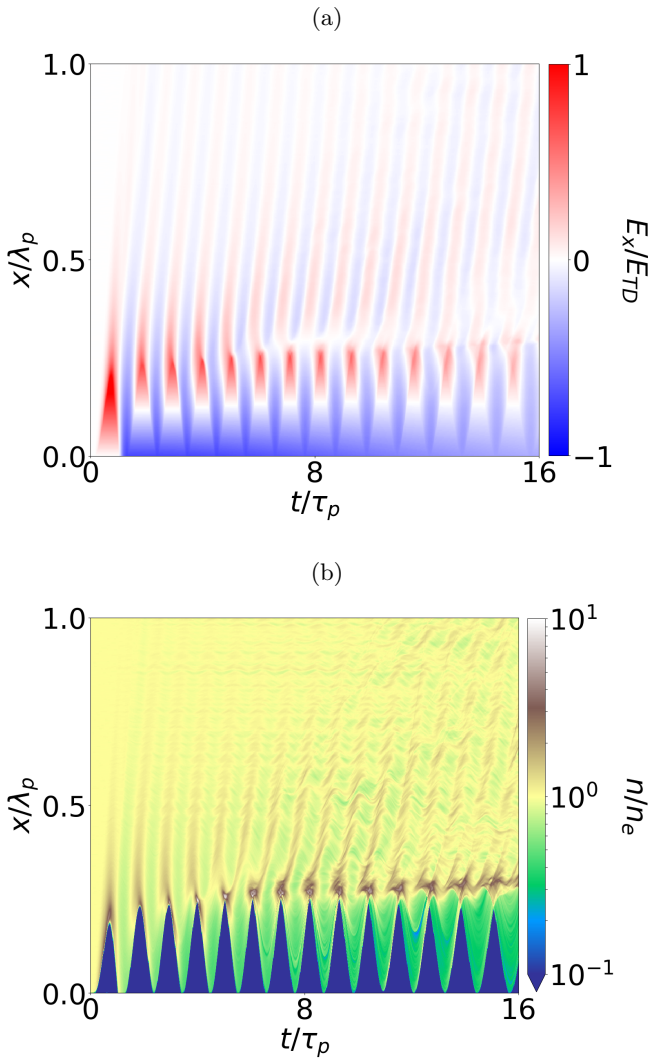

FIG. 4: The evolution in space and time of the longitudinal electric field E_x (Fig. 4a) and electron density n (Fig. 4b). The electric field is normalized with respect to the Tajima-Dawson field E_{TD}, and the electron density n is normalized to the initial uniform density n_e. The downward arrow on the color bar of Fig. 4b reflects that n extends to zero in the deep blue areas. The time domain is normalized with respect to the period of plasma oscillation, $\tau_p = 2\pi/\omega_p$.

a "darkness" metric D. This quantity D is defined as the specific momentum entropy $D = S/\langle K \rangle$, where $S = -\int_{-\infty}^{\infty} \ln[f(P_x)] f(P_x) dP_x$ is the differential Boltzmann entropy of the longitudinal momentum distribution $f(P_x)$, where $P_x = p_x/p_T$ is the longitudinal momentum normalized to the thermal momentum $p_T = \sqrt{m_e T_e}$, and $\langle K \rangle = \int_{-\infty}^{\infty} [\sqrt{1 + P_x^2/(m_e c/p_T)^2} - 1] f(P_x) dP_x$ is the average electron kinetic energy per particle normalized to $m_e c^2$ considering only the contribution from p_x. The distribution $f(P_x)$ is normalized according to $\int_{-\infty}^{\infty} f(P_x) dP_x = 1$. This index D does not take into account the dependence of the total laser energy content on the plasma wavelength λ_p; as λ_p increases for lower densities, the laser pulse length increases to maintain a resonant length. Instead, by keeping the laser always to a resonant pulse length, the plasma excitation mechanism is held constant.

For a scan over the density values $n_c/n_e \in [0.5, 14]$ at $a_0 = 1$, Fig. 5 shows the approximately final values for the index D normalized to the initial value D_0, which is the same for each data point and has an analytic form for a Maxwellian distribution. One point in the overdense regime ($n_c/n_e = 0.5$) has been added as well for cautious comparison of the "black" and super-critical regimes. As

$n_c/n_e \to \infty$, $s/s_0 \to 0$, while as $n_c/n_e \to 0$, D/D_0 climbs to a large value. These limits reflect the substantive difference in each regime. For "blue" waves, the average electron energy grows much faster than the momentum entropy, owing to the development of a typical wakefield phase-space structure. For "black" waves in contrast, disorder in phase space dominates growth in average kinetic energy and becomes ever more severe for increasing plasma density. The "darkness" index D/D_0 for "blue" waves thus asymototes to zero while that for "black" waves is characterized by finite size tending to a large value. Between these two extremes, a "grey" wave state can exist, as is shown for example in Fig. 6 for the case of $n_c/n_e = 3$, which shows both aspects of bulk flow and traditional wakefield acceleration.

This index may then provide a guide to the most appropriate regime in which to operate for a particular application. For the generation of a mono-energetic, high-energy electron beam, $D/D_0 \ll 1$ is desirable, as a "blue" wave will cleanly accelerate a small population of electrons to extremely high energy. Being mindful of the dephasing length, one can then insure that the accelerated electrons are captured at peak energy. In contrast, for some medical applications, such as in a cancer-treatment scheme where a source of radiation is brought directly to the cite of a tumor, a significant dose of low-energy (shallow-penetrating) electrons is desirable, with less constraint on the beam quality and electron energy distribution. One is attracted in this case to the "black" regime, which has $D/D_0 \sim 1$. For long, low-intensity laser pulses, as would be amenable to a fiber laser, this regime can also be accessed even at moderate plasma densities ($n_c/n_e \approx 10$) due to Raman forward scattering[33].

III. LASER INTENSITY SCALING

Apart from plasma density, the second chief parameter determining the nature of the wakefield response is the laser intensity a_0. To understand wakefield physics at high density, it is thus also necessary to understand the scaling of accelerated electron energy $\Delta\mathcal{E}$ with respect to a_0. For medical applications, it is also necessary to understand the electron energies available for various laser intensities, particularly $a_0 < 1$. Two cases are considered: the low-density case of $n_c/n_e = 10$ and the moderate-density case of $n_c/n_e = 3$. For each case a_0 is scanned logarithmically over the range $a_0 \in [0.1, 10]$ and the maximum electron energy is recorded.

The expected functional dependence of $\Delta\mathcal{E}(a_0)$ has thus far been represented simply by $g(a_0)$. Here we compare the case $g(a_0) = \sqrt{1+a_0^2} - 1$ to the results of the scan over a_0. Of particular interest for comparison with the simulation results is that this function has two slope regimes: $\ln g/\ln a_0 = 2$ for $a_0 \ll 1$ and $\ln g/\ln a_0 = 1$ for $a_0 \gg 1$.

The results of the scan are shown in Fig. 7. First for the low-density ("blue") case (Fig. 7a), the transition

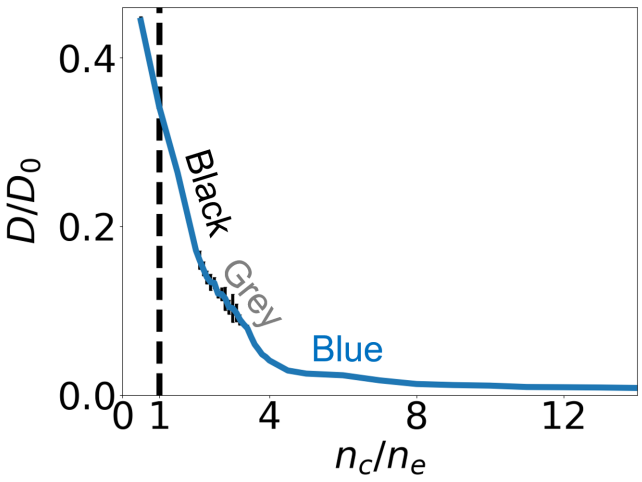

FIG. 5: The specific entropy ("darkness") index D normalized to its initial value D_0 for a scan of the density ratio values $n_c/n_e \in [0.5, 14]$ for laser intensity $a_0 = 1$ and a resonant pulse length. The plotted index is the mean of the calculated index for the last ten time steps in each run. The black error bars represent one standard deviation of this set of averaged values. Rough indications of the wave type for particular regions are given in text. Because the plasma is initialized with the same temperature in each case, the initial index D_0 is the same for every data point. The critical density is marked by a dashed line.

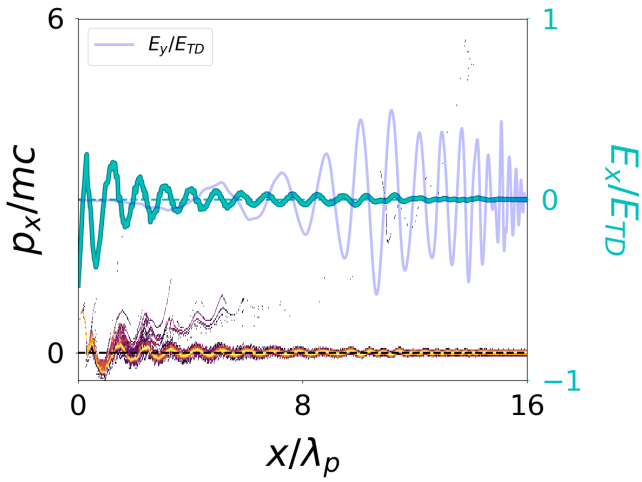

FIG. 6: The electron phase space and field structure of the intermediate ("grey") case of density $n_c/n_e = 3$ at the laser intensity $a_0 = 1$.

in slope is indeed seen, and the simulation results are in general agreement with $g(a_0)$. The moderate-density ("grey") case (Fig. 7b) also shows rough agreement with $g(a_0)$. Notably, for the low-density case, a sharp transition in maximum electron energy is seen around $a_0 = 1$. This transition may be indicative of the "switching on"

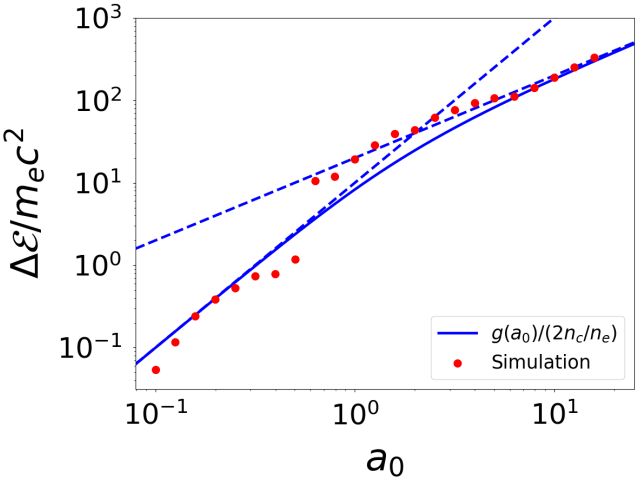

(a) E_{max} vs a_0 for fixed density ratio of 10

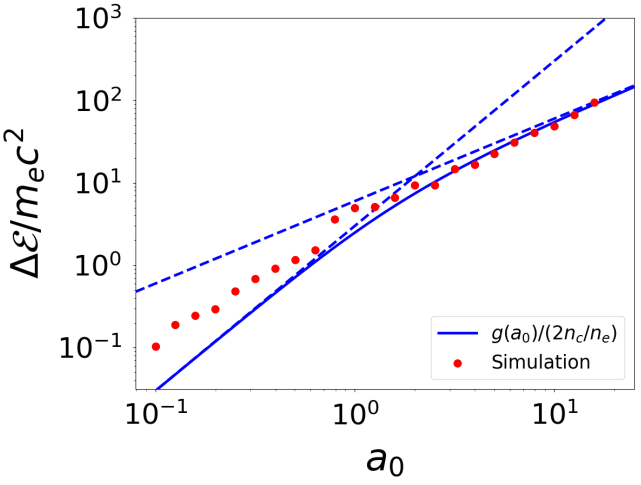

(b) E_{max} vs a_0 for fixed density ratio of 3

FIG. 7: The maximum electron energy as a function of laser intensity a_0 for two density cases: $n_c/n_e = 10$ (7a) and $n_c/n_e = 3$ (7b). The maximum energies (red dots) are compared with the function $g(a_0)$ (blue solid line). The blue dashed lines represent the asymptotic behavior of $g(a_0)$ for $a_0 \ll 1$ and $a_0 \gg 1$.

of electron trapping that occurs once the laser amplitude enters the relativistic regime at $a_0 = 1$; for $a_0 \ll 1$, substantial electron trapping does not occur for typical LWFA. In contrast, at higher density (Fig. 7b), the transition is less prominent, and electron energy for $a_0 \ll 1$ is higher than that given by $g(a_0)$. Because the electron acceleration mechanism in this regime has shifted more to the sheath acceleration typified in Fig. 3b, which does not have an intensity-based "switching on" transition, but can instead accelerate electrons even at very low intensities owing to the slow laser group velocity $v_g \lesssim v_T$, a less abrupt transition around $a_0 = 1$ in this case is expected. As an additional consequence, the sheath acceleration is able to accelerate electrons with comparative efficiency in the regime $a_0 \ll 1$, leading to the apparent acceleration enhancement above $g(a_0)$ in Fig. 7b. In the regime of very large a_0, it should also be noted that other work[34] has found that the scaling of electron energy should follow a_0^2 from ulta-relativistic effects.

These results suggest that an a_0 between 0.1 and 0.8 gives the best results for achieving electrons with $\Delta\mathcal{E} < 1$ MeV while still allowing the density ratio to be varied. In general an a_0 value greater than 1 results in greater electron energies than what we have in mind for medical applications (see section V).

IV. LONGER LASER PULSES WITH SELF-MODULATION

Thus far the simulations in this work have used resonant laser pulse lengths. Letting λ_l be the laser pulse length, a resonant pulse has $\lambda_l/\lambda_p = 0.5$. As has been mentioned previously, such a pulse can be difficult to achieve for a plasma near the critical density, requiring a single or sub-cycle laser pulse. An attractive alternative is provided by the phenomenon of self-modulation[35–37], where a large laser pulse ($\lambda_l/\lambda_p \gg 1$) becomes spontaneously broken into units of λ_p and reproduces the desired wakefield behavior. This regime is called self-modulated LWFA or SM-LWFA. For a fiber laser in particular, using a longer, low-amplitude pulse is preferable to a short, intense pulse.

To demonstrate the onset of SM-LWFA, a low-density plasma of $n_c/n_e = 10$ and $a_0 = 1$ is injected with laser pulses of various lengths, as is shown in Fig. 8. Both cases are shown at the same time step. First, a resonant pulse ($\lambda_l/\lambda_p = 0.5$) is used, and typical wakefield behavior results. (In general, for $\lambda_l/\lambda_p = 1$, the wakefield is suppressed.) For a longer pulse, such as $\lambda_l/\lambda_p = 3$, self-modulation begins to occur. The wakefield is strongest near the back of the laser pulse, as this region has been under the laser interaction longest. For an even longer pulse, $\lambda_{lp}/\lambda_p = 5$, as is shown in 8a, the self-modulation of the laser and the quality of the wakefield are further improved. Indeed, the strength of the wakefield is enhanced in the self-modulated cases compared to that of the resonant case.

This typical picture of SM-LWFA becomes somewhat modified for a high-density plasma. At the critical density the group velocity of the laser becomes zero, and thus the laser energy remains fixed where it is deposited in the electrons, as in the resonant pulse case (Fig. 3b). The total laser energy in this case is much greater than in the resonant pulse case, however, and so the interaction is much more violent. Figure 9 shows the electron phase space and field structure for $n_c/n_e = 1$ and a laser pulse length of $\lambda_{lp}/\lambda_p = 8$ for a snapshot at time $t/\tau_p = 96$, where $\tau_p = 2\pi/\omega_p$ is the plasma period. At this time the laser interaction has finished, as well as most of the electron acceleration, and thus this snapshot represents the near-final behavior. For $x/\lambda_p \gtrsim 32$ a large

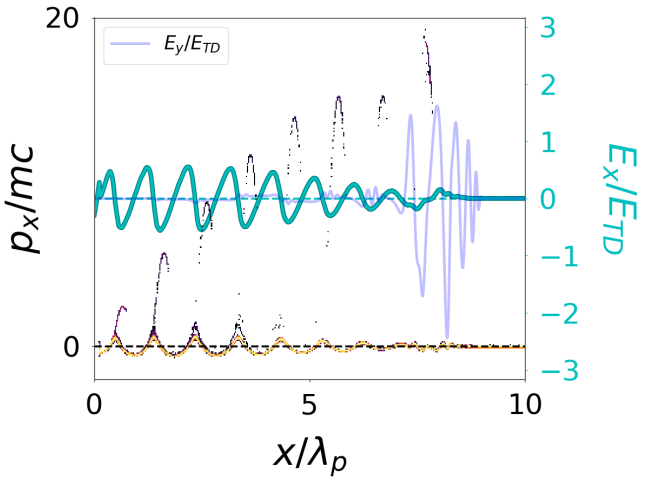

(a) $\lambda_{lp}/\lambda_p = 0.5$

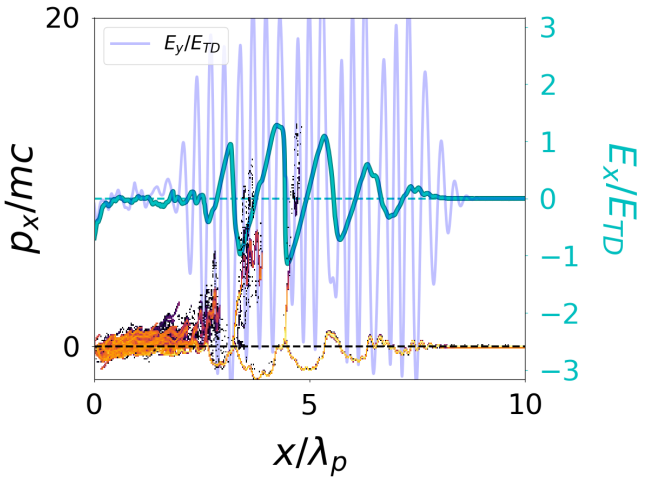

(b) $\lambda_{lp}/\lambda_p = 5$

FIG. 8: The laser pulse variation study. Comparisons of the electron phase space and longitudinal fields at density $n_c/n_e = 10$ and laser intensity $a_0 = 1$ are shown for two laser pulse lengths: $\lambda_{lp}/\lambda_p = 0.5$ (8a) and $\lambda_{lp}/\lambda_p = 5$ (8b).

body of overlapping electron streams is seen, which originate in the initial laser interaction. For $x/\lambda_p \approx 2$ a longitudinal sheath oscillation similar to that in the resonant pulse case is formed which generates subsequent electron streams. At this snapshot the total energy imparted to the electrons has converged to about 25% of the injected laser energy, which is twice that of the previous resonant pulse case in section II. In addition to better reflecting experimental reality, the use of a long (rather than resonant, sub-cycle) pulse encouragingly seems to enhance both the quantity and efficiency of low-energy electron production.

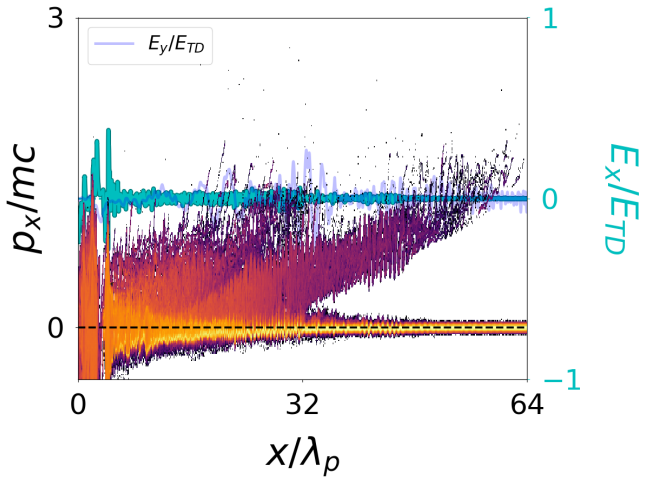

FIG. 9: The electron phase space and field structure of the critical density case $n_c/n_e = 1$ for a laser pulse of length $8\lambda_p$ at the laser intensity $a_0 = 1$, showing the buildup of a large population of low-energy accelerated electrons for the "black tsunami" regime. At this snapshot most of the electron acceleration is concluded and most of the laser has exited the domain.

V. ELECTRON TISSUE PENETRATION

We may now consider the interaction of an electron population like that in Fig. 9 with human tissue for radiation therapy. Conventional radiation therapy typically relies on exposing the body to an external source of radiation, whether X-ray, gamma-ray, protons, or electrons. In this process, the radiation passes through a significant depth of healthy tissue, causing collateral cellular damage. Two techniques to avoid this collateral damage, making use of CAN fiber lasers[16] and other related laser technologies, include intraoperative radiation therapy (IORT)[12], where the source of radiation is surgically brought to the tumor, or endoscopic radiation therapy (ESRT), where a small endoscope is internally brought to the tumor site. Consequently, in endoscopic or intraoperative therapy, the radiation produced need only penetrate a short distance, likely centimeters or less. In such a scheme, the distribution in Fig. 9, composed of low-energy electrons, may be applicable. In addition, some instances of skin cancer[38–40] may be addressed by electron radiation therapy. Specifically, for such tumors that are shallow or located in delicate areas, electrons from LWFA may have merit. For these application and others, the desired electron penetration depth is typically between microns and centimeters.

The penetration depth in human tissue can be approximated by integrating the stopping power of electrons in water, giving the stopping distance in the continuous slowing-down approximation (CSDA)[41,42]. At the critical density, the electron population in Fig. 9 has the energy distribution shown in Fig. 10a. This distribu-

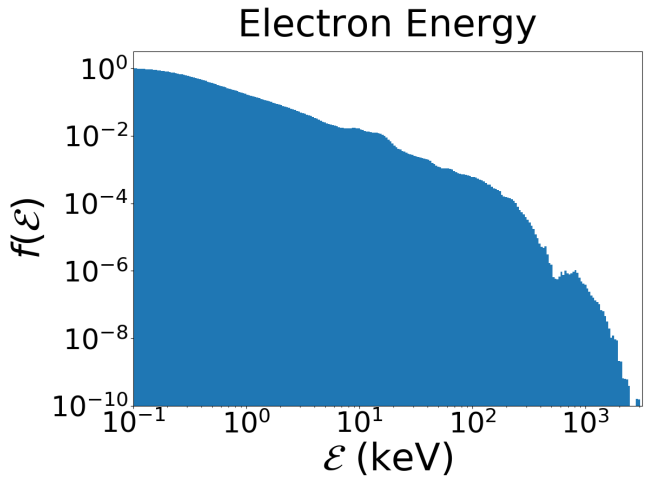

(a)

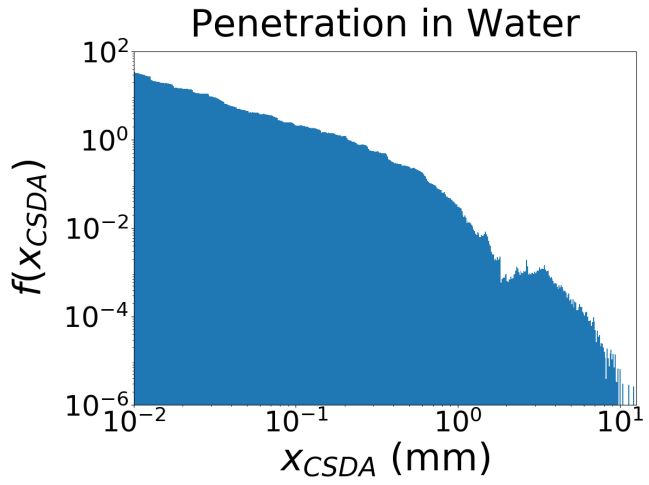

(b)

FIG. 10: Electron penetration in the high-density LWFA regime. (10a) shows the normalized electron energy distribution for the density $n_c/n_e = 1$, laser intensity $a_0 = 1$, and a pulse length of $8\lambda_p$. (10b) shows the resulting normalized distribution of electron penetration depth in the continuous slowing-down approximation (CSDA).

tion $f(\mathcal{E})$, having electrons with energies up to 1 MeV, corresponds to a maximum penetration depth x_{CSDA} in water of about $\lesssim 1$ cm, as is shown in Fig. 10b as a function of x_{CSDA}. Tuning the plasma density allows control of the penetration depth. For $n_c/n_e = 5$, the electrons produced are somewhat more energetic, and a large population can reach a penetration depth of 1 cm. At $n_c/n_e = 10$, the maximum range is on the order of centimeters. The laser intensity a_0 can also be tuned for the desired electron energies produced. To produce a penetration depth of millimeters, as might be desirable in medical applications, electrons with energies on the order of 10^2 keV are needed. As an extreme case, a high plasma density and $a_0 \ll 1$ may allow a path to the creation of electrons with energies on the order of 10 keV, producing a penetration depth on the order of microns, such as might be desired for skin treatment applications. As an additional benefit, near the critical density, a significant acceleration of the bulk population of electrons occurs, potentially creating a larger overall dose of radiation than would occur for more typical wakefield acceleration. This combination of a shallow, yet tunable, penetration may be ideal for endoscopic or intraoperative medical applications.

VI. CONCLUSIONS

The majority of efforts involving plasma wakefield acceleration have focused on producing ever higher-energy electron beams, particularly for applications in particle accelerators. Notable experiments in this area include BELLA, FACET, and AWAKE (mentioned in such as[32,43]), which aim to reach TeV energies. To reach such high acceleration gradients, experiments typically use low-density plasmas ($n_c/n_e \gg 1$) and $a_0 > 1$.

The opposite regime, that of LWFA near the critical density, remains comparatively unexplored. Nonetheless, this regime holds potential for innovative approaches in fields such as cancer therapy, in the form of LWFA-powered endoscopic electron therapy (or intraoperative radiation therapy). This regime also opens possibilities for highly localized, precise treatment of targets on the skin, such as for oncology or cosmetics, making use of extremely shallow-penetrating electrons. This latter case may be particularly tractable given the low electron energies required. Crucially in all of these applications, the source of radiation is brought close to the irradiation targets such as tissues to be treated, removing collateral damage to other tissues. Consequently the radiation need only have limited penetrative power. With electrons used as the source of radiation, the desired energies are then $\lesssim 1$ MeV, which yields a penetration depth between microns and centimeters. By tuning the laser intensity and plasma density, specific depths can be produced as desired. Here we have shown though a preliminary study that LWFA can indeed produce such electrons.

To do so, the plasma density must be close to the critical density ($n_c \sim n_e$). In this regime the group velocity of a laser pulse becomes increasingly slow, and the laser-plasma interaction range reduces nearly to a single wakefield oscillation. As a consequence of these properties, the wakefield, rather than skimming a small number of electrons from the bulk distribution and accelerating them to high energy, instead dredges somewhat more deeply from the bulk, creating an effective viscosity and momentum transport. This situation manifests as a "black tsunami" in analogy to beach wave physics and represents a qualitative departure from typical wakefield physics. Upon slowing down near the shore, the wave begins to break, creates turbulence, and dredges the sea floor, creating

a visibly black wave. Wakefield physics in the limit of $n_c/n_e = 1$ manifests in a similar way, resulting in a churning wave of relatively low-energy electrons which can then be harnessed as a beam.

The gradual transition between the "black" and "blue" wakefield regimes, corresponding respectively to high and low plasma density, has been shown, along with the linear scaling of peak electron energy. The specific entropy metric D has been proposed as a quantitative index for the regime of wakefield physics under consideration. In the low-density limit ("blue" waves), $D \to 0$, while near the critical density ("black" waves), D becomes finite, possibly tending to a large value. Furthermore, a scan of maximum electron energy $\Delta\mathcal{E}$ over a range of intensities a_0 reveals a general agreement with the function $g(a_0) = \sqrt{1+a_0^2} - 1$, derived from the ponderomotive potential, despite additional complexities and the limitations of a 1D simulation geometry. The difference in the mechanism of acceleration between the high- and low-density regimes is also manifested in the maximum electron energies attained in the two cases in Fig. 7.

The recent development of coherent networks of fiber lasers (CAN)[16] has allowed LWFA research to branch into a new field of medical applications. However, two chief limitations must be addressed for a medical fiber laser system: laser intensity and pulse length. Fiber lasers have stringent intensity limitations, with a maximum allowed individual fiber intensity likely less than 10^{14} W cm^{-2}. This limitation can be mitigated through the use of many coherently added fibers and by retreating from the critical density to a more modest plasma density (such as $n_c/n_e = 10$). Even with these factors, the ultimate intensity would likely remain in the regime of $a_0 < 1$. Limitations on pulse length are also stringent; the shortest pulse length likely achievable in a fiber laser system is around 100 fs, which is several times longer than was used in Fig. 9. Fortunately, Raman scattering effects and self-modulation may allow the "black", low-energy electron regime to be accessible for a long pulse, even at very low intensity ($a_0 \ll 1$) and low density ($n_c/n_e = 10$). Here we have shown a higher-intensity example of self-modulation for $n_c/n_e = 10$, and similar results have been shown elsewhere[44].

Other challenges remain. This work has addressed only the most fundamental aspects of LWFA near the critical density. Treatment of higher-dimensional effects such as focusing and hole-boring will be necessary for any ultimate medical application, and thus must therefore await future work. However, we emphasize that the remarkable trend in specific entropy as the plasma density approaches the critical density may not have been noticed with the inclusion of higher-dimensional effects in a mixed effort. In this sense, our study has extended the original vision of Boltzmann by his introduction of Boltzmann entropy[45]. Similarly, finding a fitting material to be irradiated will require further study, particularly of 2D and 3D effects. In absolute terms, the critical density for a 1-micron laser is approximately 10^{21} cm^{-3}. To achieve such a density, and to avoid the use of gas ionization inside the body, one possibility is the use of nanomaterials with a significantly open structure, such as carbon nanotubes[27]. Such a medium would also provide the benefit of guiding the laser and wakefield. It might also be possible to tailor the design of the nanomaterial to suit the desired plasma density. Another possible issue is that the population of accelerated electrons generated by LWFA at high density is non-monoenergic and probably of high emittance. We may also strive to further increase energy efficiency. Toward such a purpose we may wish to employ a graded density of plasma to control the phase gradation of the wakefield[46,47]. Nonetheless, interesting physics has already emerged from these efforts, and the richness of a new regime is evident.

ACKNOWLEDGEMENTS

The present paper arose from the term-project efforts of the students in the tri-campus (UCI, UCLA, UCSD) graduate physics course Special Topics in Plasma Physics PHY249, "Nonlinear Plasma Physics" (Winter, 2019), led by the instructor T. Tajima. We also tried to tie plasma physics with other disciplines such as medical physics and geophysics to broaden the students' experience in physics. The tri-campus plasma physics graduate course was launched in academic year 2018, and this course was one of three such courses. The materials are partially available on a Google Drive upon request. We are thankful for discussions with G. Mourou, J. Wheeler, J.C. Chanteloup, D. Roa, X. Yan, N. Beier, and A. Nečas. This work was partially supported by the Norman Rostoker Fund at UCI.

DATA AVAILABILITY

The data that support the findings of this study are available from the corresponding author upon reasonable request.

[1]T. Tajima, K. Nakajima, and G. Mourou, Laser acceleration, La Rivista del Nuovo Cimento **40**, 33 (2017).
[2]T. Tajima and J. M. Dawson, Laser electron accelerator, Phys. Rev. Lett. **43**, 267 (1979).
[3]D. Strickland and G. Mourou, Compression of amplified chirped optical pulses, Opt. Commun. **56**, 219 (1985).
[4]K. Nakajima *et al.*, Laser wakefield accelerator experiments using 1 ps 30 TW Nd:glass laser, in *Proceedings of International Conference on Particle Accelerators*, Vol. 4 (IEEE, Washington, DC, 1993) pp. 2556–2558.
[5]K. Nakajima *et al.*, A proof-of-principle experiment of laser wakefield acceleration, Phys. Scr. **T52**, 61 (1994).
[6]E. Fourkal, B. Shahine, M. Ding, J. S. Li, T. Tajima, and C.-M. Ma, Particle in cell simulation of laser-accelerated proton beams for radiation therapy, Med. Phys. **29**, 2788 (2002).
[7]W. Newhauser and R. Zhang, The physics of proton therapy, Phys. Med. Biol. **60**, R155 (2015).
[8]S. V. Bulanov, H. Daido, T. Z. Esirkepov, V. S. Khoroshkov, J. Koga, K. Nishihara, F. Pegoraro, T. Tajima, and M. Yam-

agiwa, Feasibility of using laser ion accelerators in proton therapy, AIP Conf. Proc. **740**, 414 (2004).
[9]T. Tajima, Prospect for compact medical laser accelerators, J. Jpn. Soc. Therp. Radiat. Oncol. **9**, 83 (1997).
[10]C. Chiu, M. Fomytskyi, F. Grigsby, F. Raischel, M. C. Downer, and T. Tajima, Laser electron accelerators for radiation medicine: A feasibility study, Med. Phys. **31**, 2042 (2004).
[11]K. K. Kainz, K. R. Hogstrom, J. A. Antolak, P. R. Almond, C. D. Bloch, C. Chiu, M. Fomytskyi, F. Raischel, M. Downer, and T. Tajima, Dose properties of a laser accelerated electron beam and prospects for clinical application, Med. Phys. **31**, 2053 (2004).
[12]A. Giulietti, N. Bourgeois, T. Ceccotti, X. Davoine, S. Dobosz, P. D'Oliveira, M. Galimberti, J. Galy, A. Gamucci, *et al.*, Intense γ-ray source in the giant-dipole-resonance range driven by 10-TW laser pulses, Phys. Rev. Lett. **101**, 105002 (2008).
[13]A. Giulietti, ed., *Laser-Driven Particle Acceleration Towards Radiobiology and Medicine* (Springer International Publishing, Switzerland, 2016).
[14]K. Nakajima, J. Yuan, L. Chen, and Z. Sheng, Laser-driven very high energy electron/photon beam radiation therapy in conjunction with a robotic system, Applied Sciences **5**, 1 (2015).
[15]K. Nakajima, Laser-driven electron beam and radiation sources for basic, medical and industrial sciences, Proceedings of the Japan Academy, Series B **91**, 223 (2015).
[16]G. Mourou, W. Brocklesby, T. Tajima, and J. Limpert, The future is fibre accelerators, Nat. Photonics **7**, 258 (2013).
[17]S. C. Wilks, W. L. Kruer, M. Tabak, and A. B. Langdon, Absorption of ultra-intense laser pulses, Phys. Rev. Lett. **69**, 1383 (1992).
[18]P. Valenta, O. Klimo, G. M. Grittani, T. Z. Esirkepov, G. Korn, and S. V. Bulanov, Wakefield excited by ultrashort laser pulses in near-critical density plasmas, in *Laser Acceleration of Electrons, Protons, and Ions V*, Vol. 11037, edited by E. Esarey, C. B. Schroeder, and J. Schreiber, International Society for Optics and Photonics (SPIE, 2019) pp. 57 – 65.
[19]T. O'Neil, Collisionless damping of nonlinear plasma oscillations, Phys. Fluids **8**, 2255 (1965).
[20]F. Mako and T. Tajima, Collective ion acceleration by a reflexing electron beam: Model and scaling, Phys. Fluids **27**, 1815 (1984).
[21]H. Lamb, in *Hydrodynamics* (Dover Publications, New York, 1945) Chap. 8.
[22]A. Pukhov and J. Meyer-ter-Vehn, Relativistic magnetic self-channeling of light in near-critical plasma: Three-dimensional particle-in-cell simulation, Phys. Rev. Lett. **76**, 3975 (1996).
[23]F. Sylla, A. Flacco, S. Kahaly, M. Veltcheva, A. Lifschitz, V. Malka, E. d'Humières, I. Andriyash, and V. Tikhonchuk, Short intense laser pulse collapse in near-critical plasma, Phys. Rev. Lett. **110**, 085001 (2013).
[24]T. Nakamura and K. Mima, Magnetic-dipole vortex generation by propagation of ultraintense and ultrashort laser pulses in moderate-density plasmas, Phys. Rev. Lett. **100**, 205006 (2008).
[25]R. A. Snavely *et al.*, Intense high-energy proton beams from petawatt-laser irradiation of solids, Phys. Rev. Lett. **85**, 2945 (2000).
[26]T. Esirkepov, M. Borghesi, S. V. Bulanov, G. Mourou, and T. Tajima, Highly efficient relativistic-ion generation in the laser-piston regime, Phys. Rev. Lett. **92**, 175003 (2004).
[27]T. Tajima, Laser acceleration in novel media, Eur. Phys. J. Spec. Top. **223**, 1037 (2014).
[28]N. V. Myung, J. Lim, J.-P. Fleurial, M. Yun, W. West, and D. Choi, Alumina nanotemplate fabrication on silicon substrate, Nanotech. **15**, 833 (2004).
[29]X. Zhang, T. Tajima, D. Farinella, Y. Shin, G. Mourou, J. Wheeler, P. Taborek, P. Chen, F. Dollar, and B. Shen, Particle-in-cell simulation of x-ray wakefield acceleration and betatron radiation in nanotubes, Phys. Rev. Accel. Beams **19**, 101004 (2016).
[30]B. Rau, T. Tajima, and H. Hojo, Coherent electron acceleration by subcycle laser pulses, Phys. Rev. Lett. **78**, 3310 (1997).
[31]M. T. Hassan *et al.*, Optical attosecond pulses and tracking the nonlinear response of bound electrons, Nature (London) **530**, 66 (2016).
[32]E. Esarey, C. B. Schroeder, and W. P. Leemans, Physics of laser-driven plasma-based electron accelerators, Rev. Mod. Phys. **81**, 1229 (2009).
[33]B. S. Nicks, T. Tajima, D. Roa, A. Nečas, and G. Mourou, Laser-wakefield application to oncology, Int. J. Mod. Phys. A **34**, 1943016 (2019).
[34]C. K. Lau, P. C. Yeh, O. Luk, J. McClenaghan, T. Ebisuzaki, and T. Tajima, Ponderomotive acceleration by relativistic waves, Phys. Rev. ST Accel. Beams **18**, 024401 (2015).
[35]N. E. Andreev, L. M. Gorbunov, A. A. Pogasova, R. R. Ramazashvili, and V. I. Kirsanov, Resonant excitation of wake fields by a laser pulse in a plasma, JETP Lett. **55**, 571 (1992), [Pisma Zh. Eksp. Teor. Fiz.55,551(1992)].
[36]J. Krall, A. Ting, E. Esarey, and P. Sprangle, Self-modulated laser wake field acceleration, in *Proceedings of the 1993 Particle Accelerator Conference*, Vol. 4 (IEEE, Washington, DC, 1993) pp. 2629–2631.
[37]A. Modena *et al.*, Electron acceleration from the breaking of relativistic plasma waves, Nature (London) **377**, 606 (1995).
[38]K. Ota, T. Adar, L. Dover, and A. Khachemoune, Review: the reemergence of brachytherapy as treatment for non-melanoma skin cancer, J. Dermatol. Treat. **29**, 170 (2018).
[39]M. Veness, D. Delishaj, E. Barnes, A. Bezugly, and A. Rembielak, Current role of radiotherapy in non-melanoma skin cancer, Clin. Oncol. **31**, 749 (2019).
[40]K. B. Garbutcheon-Singhand M. J. Veness, The role of radiotherapy in the management of non-melanoma skin cancer, Aust. J. Dermatol. **60**, 265 (2019).
[41]M. J. Berger, J. S. Coursey, and M. A. Zucker, ESTAR, PSTAR, and ASTAR: Computer programs for calculating stopping-power and range tables for electrons, protons, and helium ions (version 1.21) (1999).
[42]D. K. Brice, Stopping powers for electrons and positrons (ICRU report 37; International commission on radiation units and measurements, Bethesda, Maryland, USA, 1984), Nuclear Instruments and Methods in Physics Research Section B: Beam Interactions with Materials and Atoms **12**, 187 (1985).
[43]E. Adli *et al.*, Acceleration of electrons in the plasma wakefield of a proton bunch, Nature (London) **561**, 363 (2018).
[44]F. Salehi, A. J. Goers, G. A. Hine, L. Feder, D. Kuk, B. Miao, D. Woodbury, K. Y. Kim, and H. M. Milchberg, Mev electron acceleration at 1 kHz with $<$ 10 mJ laser pulses, Opt. Lett. **42**, 215 (2017).
[45]K. Sharp and F. Matschinsky, Translation of Ludwig Boltzmann's Paper "On the Relationship between the Second Fundamental Theorem of the Mechanical Theory of Heat and Probability Calculations Regarding the Conditions for Thermal Equilibrium" Sitzungberichte der Kaiserlichen Akademie der Wissenschaften. Mathematisch-Naturwissen Classe. Abt. II, LXXVI 1877, pp 373-435 (Wien. Ber. 1877, 76:373-435). Reprinted in Wiss. Abhandlungen, Vol. II, reprint 42, p. 164-223, Barth, Leipzig, 1909, Entropy **17**, 1971 (2015).
[46]R. Hu, H. Lu, Y. Shou, C. Lin, H. Zhuo, C. Chen, and X. Yan, Brilliant GeV electron beam with narrow energy spread generated by a laser plasma accelerator, Phys. Rev. Accel. Beams **19**, 091301 (2016).
[47]A. Döpp, C. Thaury, E. Guillaume, F. Massimo, A. Lifschitz, I. Andriyash, J.-P. Goddet, A. Tazfi, K. Ta Phuoc, and V. Malka, Energy-chirp compensation in a laser wakefield accelerator, Phys. Rev. Lett. **121**, 074802 (2018).